

## Supporting Information: Non-classical crystallization pathway of transition metal phosphate compounds

Stephanos Karafiludis<sup>1,2\*</sup>, Zdravko Kochovski<sup>3</sup>, Ernesto Scoppola<sup>4</sup>, Anika Retzmann<sup>1</sup>, Vasile-Dan Hodoroaba<sup>1</sup>, Johan E. ten Elshof<sup>5</sup>, Franziska Emmerling<sup>1,2</sup>, and Tomasz M. Stawski<sup>1\*\*</sup>

<sup>1</sup>Federal Institute for Materials Research and Testing, Richard-Willstätter-Straße 11, 12489 Berlin, Germany

<sup>2</sup>Department of Chemistry, Humboldt-Universität zu Berlin, Brook-Taylor-Straße 2, 12489 Berlin

<sup>3</sup>Department for Electrochemical Energy Storage, Helmholtz-Zentrum Berlin for Materials and Energy, Hahn-Meitner Platz 1, 14109 Berlin, Germany

<sup>4</sup>Biomaterials, Hierarchical Structure of Biological and Bio-inspired Materials, Max Planck Institute of Colloids and Interfaces, Potsdam 14476, Germany.

<sup>5</sup>MESA+ Institute for Nanotechnology, University of Twente, P.O. Box 217, 7500 AE Enschede, the Netherlands

Stephanos Karafiludis: <https://orcid.org/0000-0002-7257-6311> ;

Zdravko Kochovski: <https://orcid.org/0000-0001-8375-0365> ;

Ernesto Scoppola: <https://orcid.org/0000-0002-6390-052X> ;

Anika Retzmann: <https://orcid.org/0000-0002-0208-5453> ;

Vasile-Dan Hodoroaba: <https://orcid.org/0000-0002-7901-6114> ;

Johan E. Ten Elshof: <https://orcid.org/0000-0001-7995-6571> ;

Franziska Emmerling: <https://orcid.org/0000-0001-8528-0301> ;

Tomasz M. Stawski: <https://orcid.org/0000-0002-0881-5808> ;

Corresponding authors: \*\*[tomasz.stawski@bam.de](mailto:tomasz.stawski@bam.de) ;\* [stephanos.karafiludis@bam.de](mailto:stephanos.karafiludis@bam.de)

**Keywords:** non-classical crystallization, intermediate phases, transition metals, phosphates, liquid-liquid phase separation, amorphous phases

## List of Figures

Figure S1: Stacked diffractograms of synthesized Ni, Co and $\text{Ni}_x\text{Co}_{1-x}$ phosphate samples .....	8
Figure S2: Time-resolved pH data of different reaction runs of Ni, Co and $\text{Ni}_x\text{Co}_{1-x}$ with $x = 20\%$ , $50\%$ , $80\%$ phosphates in varying concentrations .....	9
Figure S3: Conventional TEM micrographs of Ni- and Co phosphates with BF image and associated EDS maps of the precursor Ni- or Co-phosphate phase.....	10
Figure S4: Cryo-TEM analysis and tomographic reconstructions of the amorphous Ni- and Co phosphate nanophases displayed in different angles.....	11
Figure S5: Fourier transform-infrared (FT-IR) spectra of crystalline $\text{Ni}_x\text{Co}_{1-x}$ - samples.....	12
Figure S6: Flow-through-setup sketch .....	12
Figure S7: Selected time frames in scattering/diffraction of the mixed $\text{Ni}_{50}\text{Co}_{50}$ experiment and component analysis of the fit function .....	12
Figure S8: Fitting results of the in-situ SAXS data of the Ni-experiment based on a Beaucage model	13
Figure S9: Fitting results of the in-situ SAXS data of the Co-experiment based on a Beaucage model	14
Figure S10: Fitting results of the in-situ SAXS data of the mixed $\text{Ni}_{50}\text{Co}_{50}$ -experiment based on a Beaucage model. ....	15
Figure S11: ICP-MS data of the particle-filtered solution with triplicate runs in absolute mass fractions .....	16
Figure S12: EDS maps of analyzed $\text{Ni}_x\text{Co}_{1-x}$ solids with $x = 0.1-0.9$ .....	17
Figure S13: EDS-Line Scans of analyzed $\text{Ni}_x\text{Co}_{1-x}$ solids with $x = 30$ , $x = 50$ and $x = 80$ in the experiment .....	21
Figure S14: ICP-MS data of Ni, Co and P and comparison of elemental information obtained by ICP-MS and the EDS maps of multiple grains .....	22
Figure S15: Crystal structures of M-struvite $\text{Pm}\bar{2}_1$ and M-phosphate octahydrate $C2/m$ .....	22

## List of Tables

Table S1: Settings of the ICP-MS instrument used for the quantification. ....	23
Table S2: Summarized EDS data from multiple maps of $\text{Ni}_x\text{Co}_{1-x}$ -phosphate octahydrate crystals with weight and atomic percentage of the respective element.....	23
Table S3: ICP-MS data of particle-filtered solution from crystallization experiments in triplicate runs. ....	26
Table S4: ICP-MS data of dissolved $(\text{Ni}_x\text{Co}_{1-x})_3(\text{PO}_4)_2$ crystals in triplicate runs.....	26

## Supplementary Notes

Supplementary Note 1: pH curves as a proxy for reaction progress .....	6
Supplementary Note 2: Fitting SAXS data with a simplified Beaucage model.....	7

## Supplementary Videos

Supplementary Video 1 [movie\\_Ni\\_300.s.avi](#) : 3D tomographic reconstruction of the  $\text{Ni-PO}_4$  precursor phases at  $t = 300$  s derived from cryo-TEM micrographs is shown in different orientations ( $-60^\circ < \theta < 60^\circ$ ). 360° rotation of the reconstructed object around the z-axis in the x-y-plane.

Supplementary Video 2 [movie\\_Co\\_600.s.avi](#) : 3D tomographic reconstruction of the  $\text{Co-PO}_4$  precursor phases at  $t = 600$  s, derived from cryo-TEM micrographs is shown in different orientations ( $-60^\circ < \theta < 60^\circ$ ). 360° rotation of the reconstructed object around the z-axis in the x-y-plane.

## Methods

### *X-ray diffraction*

Powder X-ray diffraction (PXRD, XRD) data from the precipitated powders were collected on a D8 Bruker Diffractometer equipped with a LYNXEYE XE-T detector. Diffraction was measured with Cu K $\alpha$  radiation (1.5406 Å, 40 kV and 40 mA) from 5-60° using a step size 0.015° (2 $\theta$ ) and a scanning time of 0.5 s per step.

### *pH measurements*

The reaction progress was followed *in-situ* by measuring pH as protons were released during precipitation (see eq. (1) and eq. (2)). The pH was continuously measured with a pH electrode connected to a data logger board “DrDAQ” time resolution of 1 s (Pico Technology, Cambridgeshire, UK) at standard ambient conditions. Prior to the experiments, the pH electrode was calibrated against buffer solutions. Approximated by multiple measurements, the absolute uncertainty in the pH range of 8 to 4 is about  $\Delta\text{pH} = \pm 0.05$ .

### *Infrared spectroscopy*

FT-IR analysis was performed on a Nicolet Nexus 670 FT-IP (Thermo Fischer Scientific) in an attenuated total reflection (ATR) mode with a “Golden Gate” sample holder. Before each measurement, the sample holder was cleaned with ethanol and acetone. Air was measured, as a background spectrum. 32 scans were taken with a resolution of 4 cm<sup>-1</sup> per sample measurement. The spectral range was set to 4000 – 570 cm<sup>-1</sup> and the spectra were recorded in an absorption mode. All spectra were acquired using the OMNIC software (v9.2).

### *SEM/EDS*

The scanning electron microscopy (SEM) analysis was performed on an FEI XL 30 tungsten cathode scanning electron microscope operating with 20 keV acceleration voltage and using a secondary electron (SE) detector. Before the analysis, all samples were coated with a 30 nm-thick layer of gold.

The EDS analyses and the SEM imaging of the Ni<sub>x</sub>Co<sub>1-x</sub>-mixtures were performed under Zeiss Supra 40 (Zeiss, Oberkochen, Germany) equipped with a Schottky-field emitter. All samples were coated with carbon before analysis. A 5 kV beam voltage was applied for the imaging of all samples. An energy-dispersive X-ray (EDS) system of type UltraDry SDD (Silicon Drift Detector) with a nominal crystal area of 100 mm<sup>2</sup> from Thermo Fisher Scientific (Waltham, MA, USA) was used for the qualitative and quantitative analyses of the elemental composition. For this, highly flat sample areas (10  $\mu\text{m}$  x 10  $\mu\text{m}$ ) were selected for an EDS quantitative analysis with the software Pathfinder (v. 1.3, 2018). The corresponding EDS spectra were collected at 15 keV and a standardless quantification was performed. Due to the rough sample surface morphology, the obtained elemental compositions are estimated to exhibit an error of <10% atom. based on multiple measurements. However, quantitative comparisons of the relative results for different samples obtained under the same experimental conditions (including sample geometries) are more accurate than the absolute values. Qualitative EDS maps were acquired over selected individual crystals indicating the spatial distribution of the elements.

### *Conventional TEM*

Conventional (i.e. particles directly exposed to high vacuum) transmission electron microscopy (TEM) images were obtained on a Talos F200S Microscope (Thermo Fisher Scientific) operating at 200 kV. The Ceta 16M camera (TEM mode) and a HAADF (high-angle annular dark field) detector (STEM mode; Scanning TEM) were used to capture the images. Additionally, to collect detailed elemental information, energy dispersive X-ray spectroscopy (EDS) was performed by two side-entry retractable silicon drift detectors (SDD). A counting time of 60 s was applied for point measurements while for the elemental maps 40-50 frames were taken resulting in a counting time of 1 hour. The specimen was

prepared by mixing the 100  $\mu\text{l}$  of reactant solutions in an Eppendorf tube (1.5 ml) for 5 seconds of reaction time and dropping 10  $\mu\text{l}$  of the sample solution onto a 3 mm holey carbon-coated Cu-grid (Lacey Carbon, 400 mesh). Then, the specimens were left to dry at room temperature for 5 minutes.

### *Cryo-TEM*

Cryo-EM imaging was performed with a JEOL JEM-2100 transmission electron microscope (JEOL GmbH, Echting, Germany). Specimens were prepared by casting a 4  $\mu\text{l}$  droplet of sample solution onto lacey carbon-coated copper TEM grids (200 mesh, Electron Microscopy Sciences, Hatfield, PA) and plunge-freezing them into liquid ethane using an vitrobot (FEI Mark IV) set at 4 °C and 95% humidity. Vitrified grids were either transferred directly to the microscope's cryo-transfer holder (Gatan 914, Gatan, Munich, Germany) or stored in liquid nitrogen. All grids were glow-discharged before use. Imaging was carried out at temperatures around -180°C. The TEM was operated at an acceleration voltage of 200 kV, and an objective lens defocus of about 1.5 – 2  $\mu\text{m}$  was used to increase the contrast. Micrographs were recorded with a bottom-mounted CMOS camera (TemCam-F416, TVIPS, Gauting, Germany). Each micrograph's electron dose was kept below 20  $e^-/\text{\AA}^2$ . The tilt-series of colloidal nanophases were captured using a Serial-EM acquisition software package<sup>1</sup> with a tilt range of  $\pm 60^\circ$  and  $2^\circ$  angular degree increment at a magnification of 30k x, resulting in a pixel size of 3.6  $\text{\AA}$  at the specimen level. The alignment of the tilt-series was performed using patch tracking and then reconstructed using weighted back-projection with the IMOD software package 3. Surface segmentation was carried out using Amira (FEI Company, Eindhoven, The Netherlands). Three-dimensional surface renderings and movies were generated with UCSF Chimera<sup>2</sup>. Videos of the tomographic reconstruction of the Ni- and Co-PO<sub>4</sub> precursors based on the cryo-TEM micrographs in different orientations can be found in the electronic supplementary information.

### *In-situ SAXS/WAXS*

In situ and time-resolved small- and wide-angle X-ray scattering (SAXS/WAXS) measurements were performed in a PEEK flow-through cell coupled with a pump setup at the mySpot beamline (BESSY-II, Helmholtz Centre Berlin for Materials and Energy Berlin, Germany). Experiments were performed using a monochromatic X-ray beam at 18 keV ( $\lambda = 0.689 \text{ \AA}$ ) aligned with a capillary (borosilicate glass, Glass Müller, Berlin ID = 1.498 mm). All the samples and backgrounds were measured with this setup. A fixed volume of 100 ml of the 0.1 M DAP solution was stirred (400 rpm) in a 200 ml glass reactor. The reactor content was continuously circulated through a borosilicate glass capillary cell (ID = 1.498 mm), using a peristaltic pump (Longer BT100-2J) at 300 ml/min, (dead volume of tubing was  $\approx 2 \text{ ml}$ ). The other reactant, 100 ml of a transition metal sulfate solution, was injected into the reactor containing DAP at 300 ml/min using a second peristaltic pump with a remote control for the injection duration of  $\approx 10 \text{ s}$ . Therefore, both reactants summed in all experiments to 200 ml reaction volume. In a typical experiment, firstly the DAP solution was cycled in the flow-through setup and measured in the first frames. After several seconds, the injector metal sulfate solution was added resulting in the precipitation of transition metal phosphates. The scattering data were collected at 10 s/frame. Together with scattering, the pH measurements (DrDAQ data logger board, PicoLog 6 software) were performed every 1 s continuously for the entire duration of the experiment. The time scales of all the measurements/experiments were aligned according to the following convention: the measurement starting at  $t = 0 \text{ s}$  represents a structure of an unmixed solution (i.e. only DAP) while after the metal-bearing solution was injected. The scattering data were collected on a Dectris Eiger 9M (Pixel array  $3108 \times 3262$  pixels, pixel size  $75 \times 75 \text{ }\mu\text{m}$ ) detector. Transmission through the sample was calculated using an X-ray fluorescence signal collected from a lead beamstop using a RAYSPEC Sirius SD-E65133-BE-INC detector equipped with an 8  $\mu\text{m}$  beryllium window, where the incoming beam intensity was monitored and normalised using an ion chamber. The sample-to-detector distances allowed for a  $q$ -range of  $0.05 < q < 40 \text{ nm}^{-1}$ , a combined interval for SAXS and WAXS. The scattering  $q$ -range at small angles was calibrated against crystalline quartz and the intensity was calibrated to absolute units

against water (at 20 °C). The recorded 2D scattering data were reduced, where the reduction steps involved data normalizations and instrumental corrections, correction for transmission, subtraction of a background (an empty capillary), followed by integration to 1D scattering curves. The data sets were fitted (eq. S1) in Python using Imfit package <sup>3</sup>.

### ICP-MS

Inductively coupled plasma mass spectrometry (ICP-MS) analysis was performed on aqueous solutions and the final crystalline solids of the crystallization experiment. The same flow-through setup equipped with a pH electrode was used as in the in-situ SAXS/WAXS experiments to ensure comparability between the two approaches.

Consumables (15 mL tubes, 50 mL tubes, pipette tips, syringes) were cleaned with diluted double-sub boiled nitric acid ( $w = \text{ca. } 3\%$ , Sigma Aldrich) before the analysis. Type I reagent-grade water (18.2 MΩ cm) was obtained from a Milli-Q Integral water purification system (Merck-Millipore, Darmstadt, Germany). Analytical reagent-grade nitric acid ( $w = 65\%$ , Merck-Millipore) was purified by double sub-boiling using a sub-boiling distillation system.

The sampled solutions extracted after selected reaction times were pushed through a particle filter for probing the supernatant composition in each experiment run. Simultaneously pH was measured in-situ to better correlate the results with the synchrotron experiments (Figure 5, SI: *Methods: ICP-MS*, Figure S11). Approximately 1 ml of the solution at a given reaction time ( $t = 180 \text{ s}$  to  $t = 14400 \text{ s}$ ) was extracted and filtered using a 5 ml syringe (NORM-JECT®) and hydrophilic filters (pore size =  $0.45 \mu\text{m}$ , CHROMAFIL®). Then, 500  $\mu\text{L}$  of the filtrate were acidified to  $w = 3\%$  using double-sub boiled nitric acid ( $w = 65\%$ ). ICP-MS measurements of the samples were carried out after the dilution by a factor of 10000 with diluted nitric acid ( $w = 3\%$ ).

The final precipitated solids were collected onto a cellulose filter (pore size  $0.45 \mu\text{m}$ , LABSOLUTE) by using a vacuum filtration kit (i.e. Büchner funnel). Afterward, the powders were washed with distilled water and left to dry in air at room temperature for several hours. Furthermore, for the exclusion of heterogeneity effects and probing at a larger scale, elemental bulk ICP-MS analysis was performed on dissolved crystals. In such a way, we could obtain elemental information complementary to the EDS measurements of the solids (SI: Figure S14). For the actual measurement of the solids, around 0.02 mg of the dried solid powders weighed and dissolved in diluted  $w = 2\%$  double sub-boiled nitric acid ( $w = 65\%$ ). Multi-elemental analyses (incl. P, Co, and Ni) of the filtrates were performed using an ICP-MS (ICAP-Q, Thermo Scientific, Bremen, Germany) coupled to an ESI SC-4 DX FAST autosampler (Elemental Scientific, Omaha, USA). The ICP-MS instrument was optimized in STD mode in a daily routine using a tuning solution (Thermo Scientific) to obtain maximum signal intensity while maintaining high stability and low oxide and double-charged rates. General instrumental settings for the multi-elemental measurements are described in Table S1.

The multi-elemental quantification of the filtered liquids was accomplished by external calibration (9-point calibration ranging for Co and Ni from  $0.1 \text{ ng g}^{-1}$  to  $150 \text{ ng g}^{-1}$  and for P from  $10 \text{ ng g}^{-1}$  to  $15000 \text{ ng g}^{-1}$ ) with standards prepared gravimetrically from a multielement stock solution (ICP multielement standard Merck VI, 30 Elements in nitric acid  $10\text{--}1000 \text{ mg L}^{-1}$ ) and P stock solution (ICP Standard, Merck-Millipore) including  $1 \text{ ng g}^{-1}$  indium (prepared from an In stock solution, Merck-Millipore) as internal normalization standard. Furthermore, the performance of the multi-elemental analysis was monitored with an in-house quality control solution (incl. P, Co and Ni) prepared in nitric acid ( $w = 2\%$ ). The Limits of Detection (LOD) and Limits of Quantification (LOQ) were calculated according to DIN ISO 11843-2<sup>4</sup>. Therefore, the LOD is defined as a 3-fold standard deviation of the blank and the LOQ is defined as a 10-folds standard deviation of the blank. Total combined uncertainties for multi-element analysis were calculated using a simplified Kragten approach<sup>5</sup>.

### Supplementary Note 1: pH curves as a proxy for reaction progress

Due to the release of protons during the precipitation reactions (eqs. S1, S2), pH can serve as a proxy for reaction progress in the Ni, Co, and  $\text{Ni}_x\text{Co}_{1-x}$  phosphate samples. Initially, the pH was  $\sim 8.0$  for the 0.1 M DAP solution and  $\sim 5.7$  for both  $\text{NiSO}_4$  and  $\text{CoSO}_4$  solutions at 0.1 M. When metal salt and DAP were mixed, near-instantaneous precipitation was observed in both transition metal systems, which correlated with the simultaneous drop in pH. The initial pH of the 0.02 M single or two-metal-cation sulfate solutions was 5.9 (Ni, Co and  $\text{Ni}_x\text{Co}_{1-x}$ ) for the low concentration runs (SI: Figure S1A and S1B). In all systems, M-struvite formed within several minutes. The pure Ni-sample precipitated slightly faster than the Co-containing  $\text{Ni}_x\text{Co}_{1-x}$  and pure Co samples in the low concentrated metal systems of  $c(\text{M}^{2+}) = 0.02 \text{ M}$  while the pH drop occurred in the first 100 s. Higher Co content in the low-concentration  $\text{Ni}_x\text{Co}_{1-x}$  mixtures, led to the progressive increase in the reaction time (SI: Figure S1A and S1B).

In the highly concentrated system, 0.1 M DAP solution was also used. Immediately after mixing both 0.1 M solutions, the pH dropped to around  $\sim 5.8$  for all systems. While the pH of the 0.1 M Ni sample declined slightly over the first 50 - 150 s to a stable plateau value of 5.8, the pH for 0.1 M Co reached nearly instantaneously a plateau value of 5.9 and stagnated until around 1500 s. After 1500 s a significant pH jump to a value of 4.6 over 500 s occurred in the 0.1 M Co sample which was most likely related to the transformation of the colloidal phases as the color changed simultaneously from purple to light pink. A progressive increase of Co from 0.02 M to 0.1 M changed the decline in pH significantly in values (more acidic) and a trajectory (SI: Figure S1C and S1D). The different shapes of the pH decline are directly associated with the stable Co-phase (Co-struvite  $c(\text{Co}) < 0.04 \text{ M}$ , Co-phosphate octahydrate  $c(\text{Co}) > 0.06 \text{ M}$  or both at  $0.04 \text{ M} < c(\text{Co}) < 0.06 \text{ M}$ ) and the related life-time of the amorphous phases. Interestingly, in the high concentrated two-metal-cation  $\text{Ni}_x\text{Co}_{1-x}$  mixtures of  $c(\text{M}^{2+}) = 0.1 \text{ M}$  with  $x = 20\%$ ,  $50\%$ ,  $80\%$ , the combination of two metals in different ratios enlarged the equilibrium time starkly. While the  $\text{Ni}_{80}\text{Co}_{20}$  mixture with  $c(\text{M}^{2+}) = 0.1 \text{ M}$  looks similar to the pure Ni sample, the Co-rich mixtures ( $x = 50\%$  and  $80\%$ ) deviate in their reaction progress from the pure Co case (equilibrium times:  $t_{\text{eq}}(\text{Ni}_{50}\text{Co}_{50}) = 3 \text{ h}$ ,  $\text{Ni}_{20}\text{Co}_{80}$  around  $t_{\text{eq}}(\text{Ni}_{20}\text{Co}_{80}) = 80 \text{ min}$  compared to  $t_{\text{eq}}(\text{Co}) = 40 \text{ min}$ ). In such a way, the reaction progress can be varied in the two-metal mixtures through different ratios of Ni and Co.

In summary, the Ni- struvite formation reaction proceeds fast within the first 100 - 150 s, while the Co-phosphate reactions exhibit much longer reaction times (400 s for 0.02 M and around 3000 s for 0.1 M  $\text{Co}^{2+}$ ) due to the preservation and transformation of long-lived colloidal phases.

In an extreme concentrated run, the initial pH of the 1 M DAP solution did not differ significantly from the 0.1 M concentrated solution with a value of  $\sim 8.05$ . When the equimolar concentrated metal solution was added, the pH dropped for Ni to 4.7 while in the Co-containing samples a plateau value was reached at around the same value. After extended reaction times the plateau value sank within a second decline to 3.7. While the Ni sample reached equilibrium already after several minutes and the Co samples after one and half hour, the  $\text{Ni}_{50}\text{Co}_{50}$ -mixture required more than six hours to equilibrate. Thus, the life-time of the amorphous colloidal nanophases is dependent on the concentration and the molar ratio of the two transition metals. These pH data exemplify the complex nature of the amorphous phases and their sensitivity to changes of the reaction parameters such as the involved metal(s) species and their concentrations.

## Supplementary Note 2: Fitting SAXS data with a simplified Beaucage model

The measured in-situ SAXS/WAXS data of TMPs crystallization experiments were fitted with a 2-level unified scattering function (Beaucage model)<sup>6,7</sup>. The unified scattering function was proposed in 1995<sup>6</sup> as a universal approach to fit SAXS data in disordered systems with hierarchical structures. Hierarchical structures consist of a variety of particle sizes and shapes such as nanoparticles (scattering at high  $q$ ) which aggregate to clusters on the mesoscale (scattering at medium  $q$ ) and finally condensate to large  $\mu\text{m}$ -scale sized frameworks (scattering at low  $q$ )<sup>8</sup>. It is assumed that each “size-level” of particles will contribute to a different part of scattering curve, within some  $q$ -range, and the levels will overlap with each other in the small-angle scattering pattern. Accordingly, the Beaucage function was derived as a linear combination of multiple scattering functions, each describing scattering signals in a restricted  $q$ -range. It combines Porod’s law<sup>9,10</sup>, Guinier law<sup>11</sup> combined with a crossover error function for different structural levels to fit scattering signals at low, medium and high  $q$ .

$$I(q) = \sum_{i=1}^n [G_i e^{-\frac{q^2 R_{g,i}^2}{3}} + B_i e^{-\frac{q^2 R_{g,i+1}^2}{3}} q_i^{*P_i}] \quad (\text{S1})$$

with

$$q_i^* = \frac{\text{erf}\left(\frac{q R_{g,i}}{\sqrt{6}}\right)^3}{q}$$

Here,  $G_i$ , the classical Guinier pre-factor corresponding to  $G_i = N_p \Delta \rho^2 V^2$ , describes an exponential decay of scattering at a characteristic size the radius of gyration  $R_g$  for one structural level  $i$ .  $B_i$  represents a pre-factor to a type of power-law scattering scaling with the surface or mass fractal exponent  $P_i$ . In surface fractals such as crystal interfaces  $P_i$  exhibits values typically  $> 3$  and  $< 4$ , while in mass fractals such as the framework of the amorphous phases,  $1 < P_i < 3$ . A crossover between those functions is accomplished by inserting an error function. Based on eq. S1, we assumed two structural levels (eq. S2). The first structural level is based on the building blocks or primary amorphous particles with a smallest radius of gyration  $R_{\text{sub}}$ . The second structural level is originating from the agglomerated colloidal frameworks of these primary particles with a radius of gyration of  $R_g$ . Thus,  $R_g > R_{\text{sub}}$ .

$$I(q) = G e^{-\frac{q^2 R_g^2}{3}} + B e^{-\frac{q^2 R_{\text{sub}}^2}{3}} q_1^{*P} + G_{\text{sub}} e^{-\frac{q^2 R_{\text{sub}}^2}{3}} + B_{\text{sub}} e^{-\frac{q^2 R_{\text{sub}}^2}{3}} q_2^{*P_{\text{sub}}} + bkg \quad (\text{S2})$$

with

$$q_1^* = \frac{\text{erf}\left(\frac{q R_g}{\sqrt{6}}\right)^3}{q} \quad q_2^* = \frac{\text{erf}\left(\frac{q R_{\text{sub}}}{\sqrt{6}}\right)^3}{q}$$

The selected fits and the evolution of the fitting parameters can be found in this ESI (ESI: Figure S8, S9 and S10). For a better understanding of the contribution of each term to the overall fitting curve, a component analysis was performed on an exemplary data frame in the mixed  $\text{Ni}_{50}\text{Co}_{50}$  experiment (Figure S7). In sum, the fits and the measured datasets are well in agreement. A detailed view of the fitting results can be seen in Figure S8, Figure S9 and Figure S10. Although the observed trends in the fitting parameters seem to be sufficient and meaningful, we want to mention that the Beaucage model exhibits some limitations. As it is primarily focussed on fitting hierarchical structure, fractal and particulate particles, it assumes a constant electron density in all observed chemical entities (particles, agglomerates, crystals). This is a simplification considering our data, because in the course of condensation and densification the electron density can change throughout the particle growth. Moreover, since the Beaucage function fundamentally relies on Guinier approximation, it cannot correctly for polydispersity. However, although this model does not consider all scattering features precisely, it offers a practical approach for the quantification of evolutionary trends in hierarchical structures.

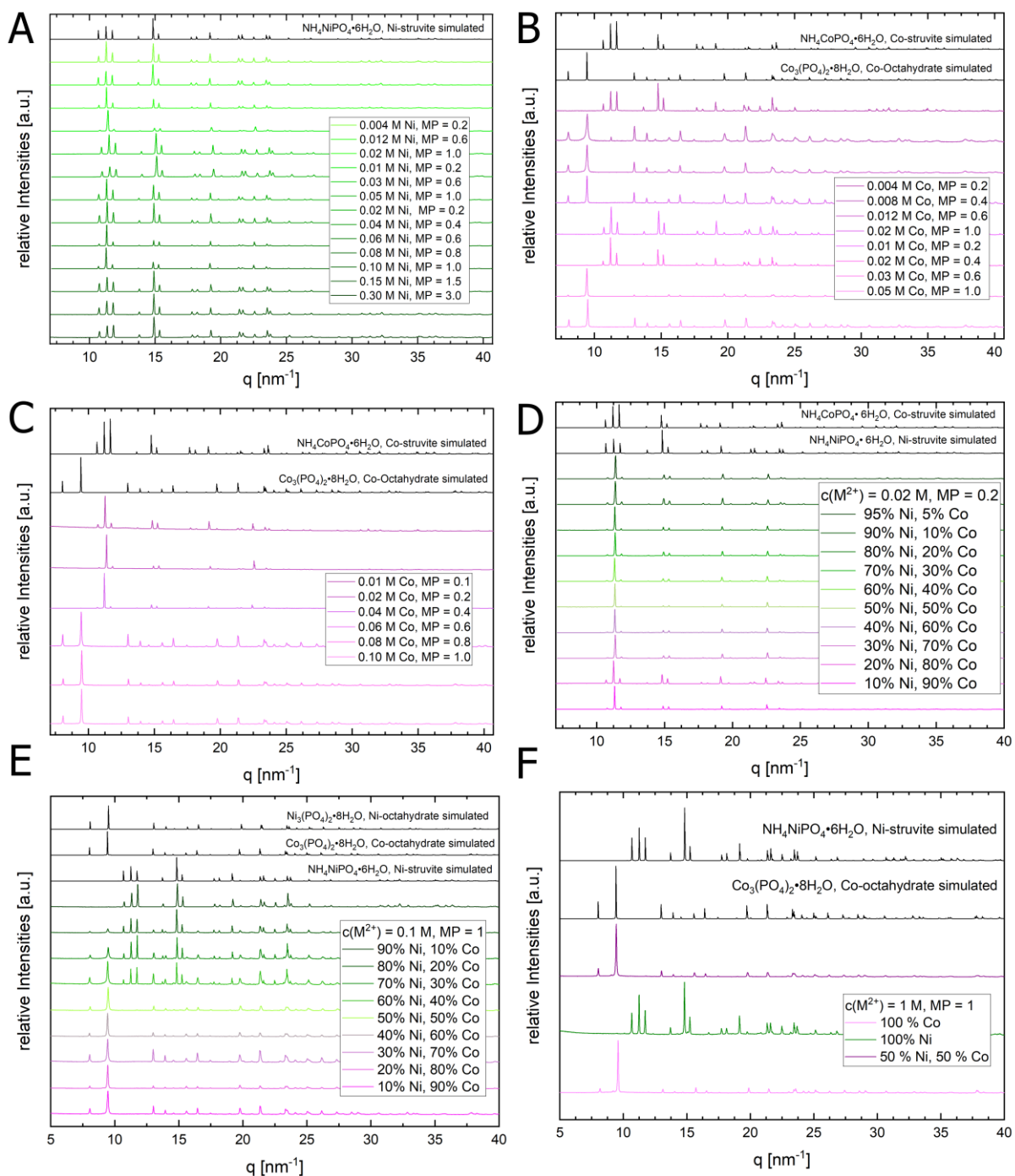


Figure S1: Stacked diffractograms of Ni-Co phosphates synthesized for different reaction conditions with the simulated pattern of the phosphate compound in black. MP represents the M/P ratio in the solution. Ni-struvite reference ICSD 403058; Co-struvite reference ICSD 170042; Co(II) phosphate octahydrate reference COD 2020362; Ni(II) phosphate octahydrate reference ICSD 240946



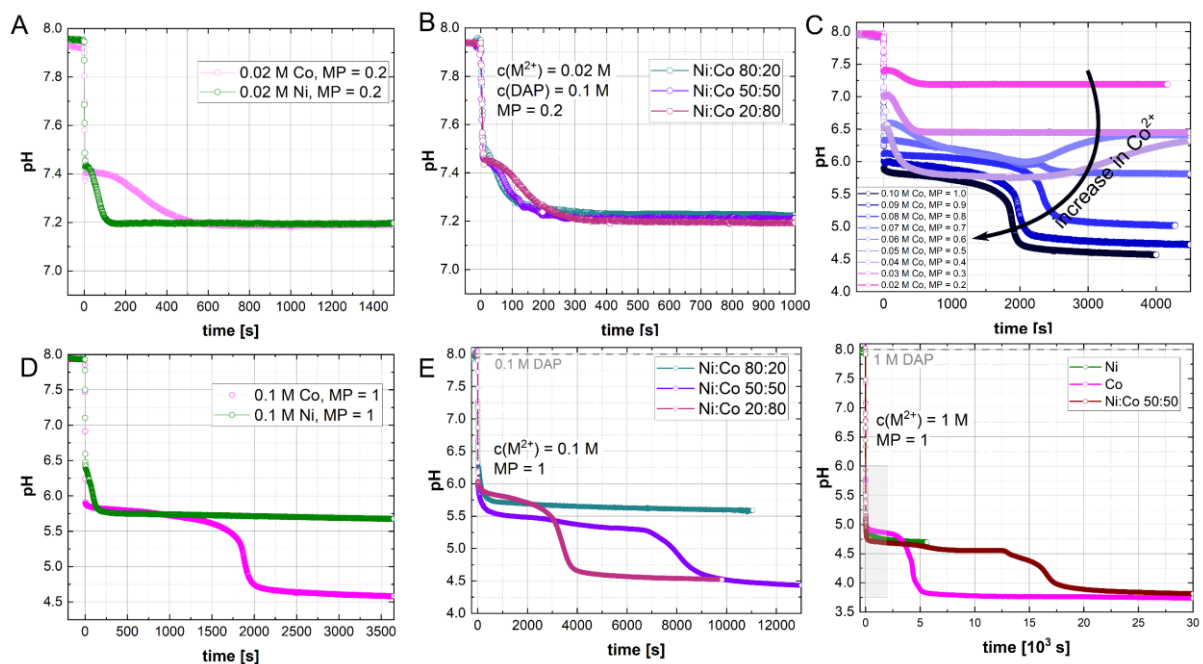


Figure S2: Time-resolved pH data of different reaction runs of Ni, Co and  $\text{Ni}_x\text{Co}_{1-x}$  with  $x = 20\%$ ,  $50\%$ ,  $80\%$  phosphates in varying concentrations. If not differently stated,  $0.1 \text{ mol/l}$  DAP ( $\text{pH} \approx 8.0$ ) was used as the starting reactant. (A, B) The pH data of pure Ni and Co samples in low metal concentrations of  $0.02 \text{ M}$ . (C) The pH data of pure Co samples in varying metal concentrations from  $0.02 \text{ mol/l} < c(\text{Co}^{2+}) < 0.1 \text{ mol/l}$ . The pH data of (D) Ni, Co and (E)  $\text{Ni}_x\text{Co}_{1-x}$  samples with  $x = 20\%$ ,  $50\%$  and  $80\%$  samples in high concentration runs of  $c(\text{M}^{2+}) = 0.1 \text{ mol/l}$  are displayed. (F) The pH data of extreme concentration run of pure Ni, pure Co and mixed  $\text{Ni}_{50}\text{Co}_{50}$  samples with  $c(\text{M}^{2+}) = c(\text{DAP}) = 1 \text{ mol/l}$  through time.

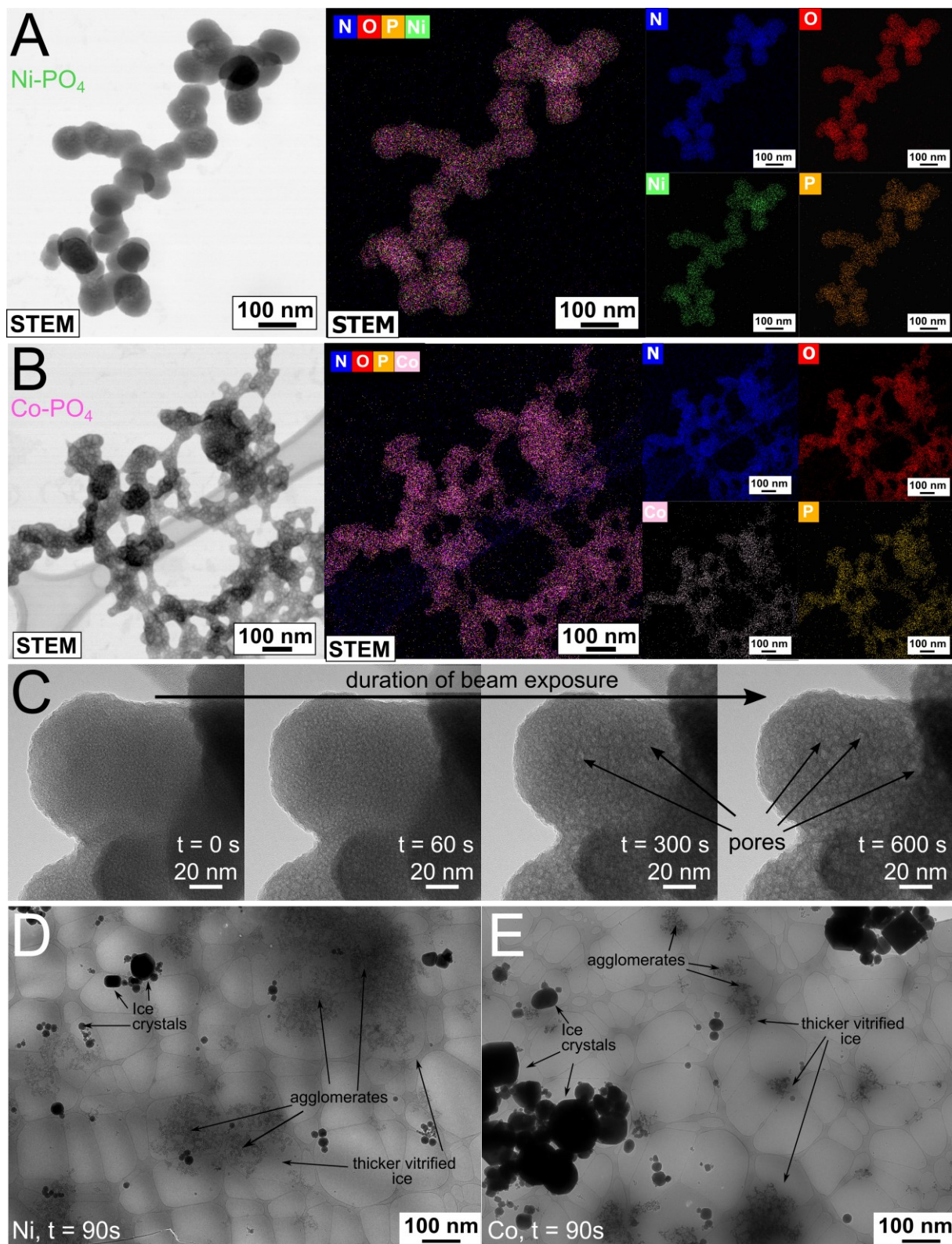


Figure S3: Conventional TEM micrographs of (A) Ni- and (B) Co phosphates with BF image and associated EDS maps of the precursor Ni- or Co-phosphate phase (blue N, red O, orange P, green Ni, pink Co). (C) A detailed view of the Ni-phosphate precursor is displayed showing its decomposition under a prolonged beam exposure in conventional TEM. The intermediate phases degas ammonia and water resulting in the formation of pores. (D) Overview cryo-TEM image of Ni sample at t = 90 s with arrow-marked features are displayed observable in the micrograph. (E) Overview cryo-TEM image of Co sample at t = 90 s with arrow-marked features observable in the micrograph.



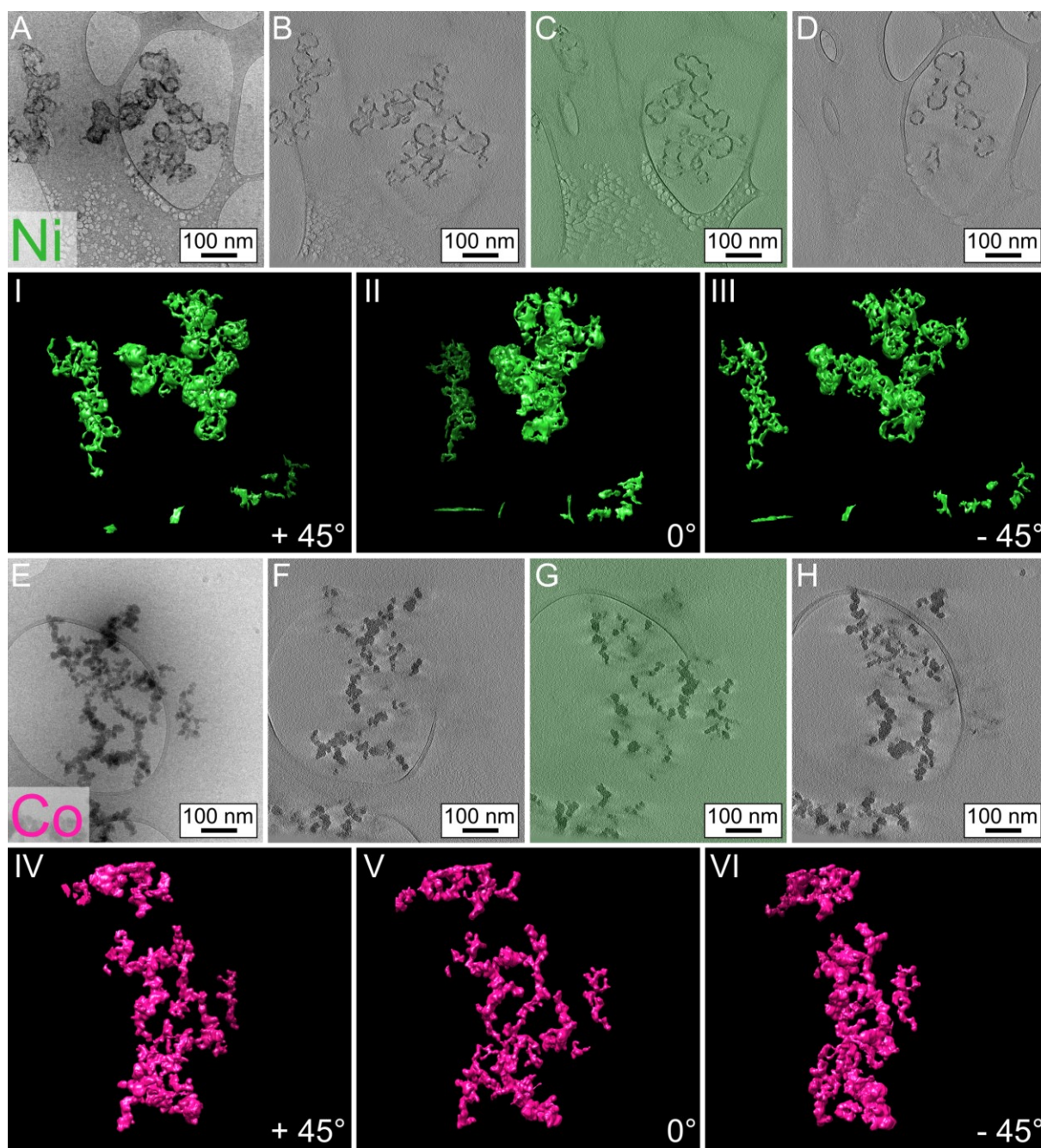


Figure S4: Cryo-TEM analysis of the amorphous Ni- and Co phosphate nanophases at  $t = 5$  min (Ni, green) and  $t = 10$  min (Co, pink): (A) The original bright-field cryo-TEM image of the Ni-PO<sub>4</sub> sample, (B-D) selected XY slices through the tomographic reconstruction of an selected Ni-PO<sub>4</sub>-particle. (E) The original bright-field cryo-TEM image of the Co-PO<sub>4</sub> sample, (F-H) Selected XY slices through the tomographic reconstruction of a selected Ni-PO<sub>4</sub>-particle. The highlighted green slice in (C) for Ni-PO<sub>4</sub> and (G) for Co-PO<sub>4</sub> corresponds to the central slice (0°). Three-dimensional particle surface renderings in selected angles from  $+45^\circ < 0^\circ < 45^\circ$  are displayed (I, II, III for Ni-PO<sub>4</sub> and IV, V, VI for Co-PO<sub>4</sub>). Videos of the tomographic reconstruction of the Ni- and Co-PO<sub>4</sub> precursors based on the cryo-TEM micrographs in different orientations are attached in the electronic supplementary information.

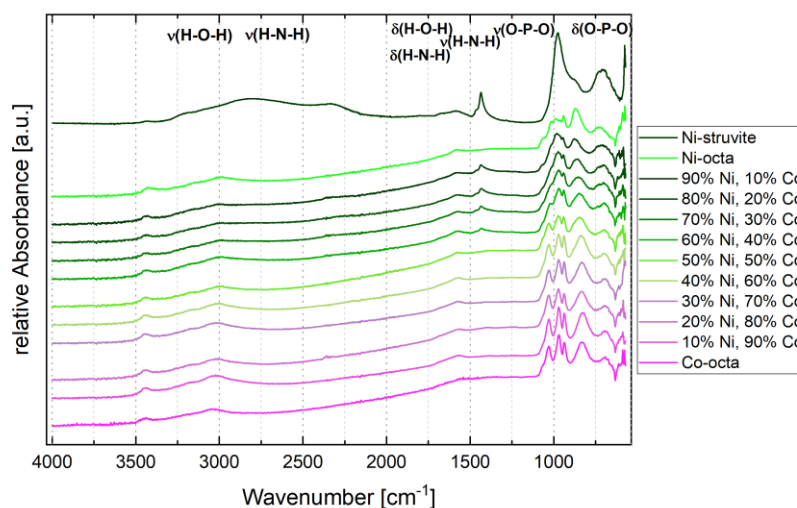


Figure S5: Fourier transform-infrared (FT-IR) spectra of crystalline  $\text{Ni}_x\text{Co}_{1-x}$  sample and phosphate octahydrate in comparison with the amorphous  $\text{Ni-PO}_4$  phase.

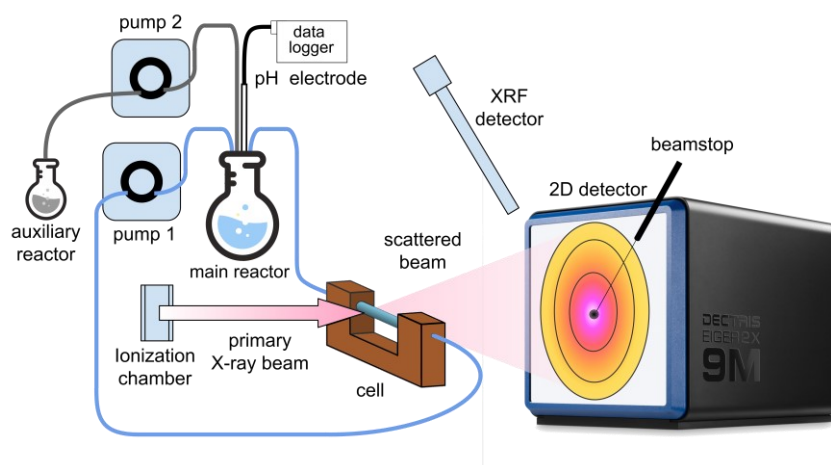


Figure S6: Flow-through-setup sketch shows the general configuration: a main reactor (main cycle) attached with a borosilicate glass capillary and an auxiliary reactor (injection cycle); As the beam is transmitted through the filled capillary and resulting scattered signal is measured by the 2D detector.

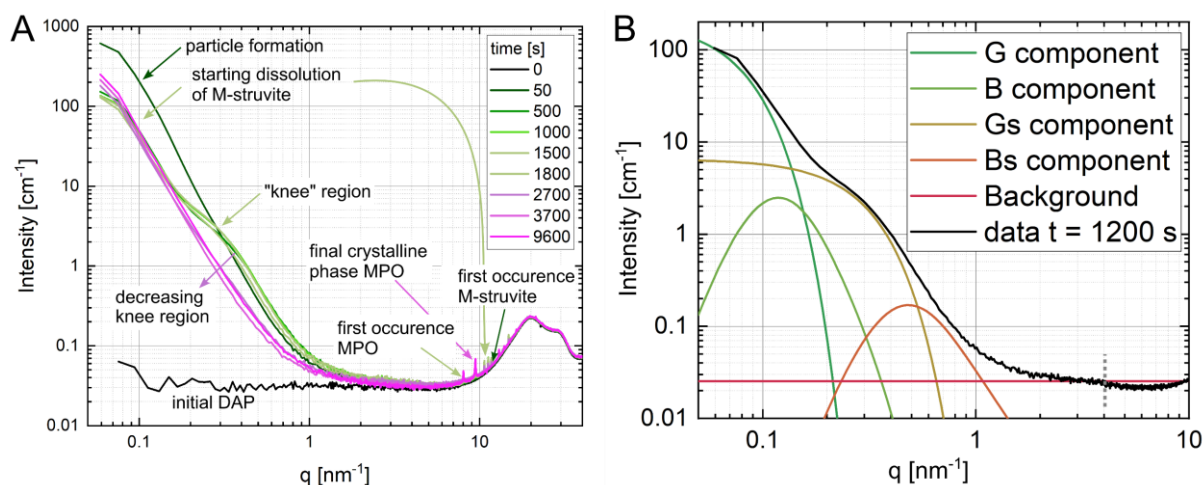


Figure S7: (A) Selected time frames in scattering/diffraction of the mixed  $\text{Ni}_{50}\text{Co}_{50}$  experiment are displayed. Colored arrows mark the distinctive time of the crystallization event. (B) Component analysis of the fit function associated with the parameters  $G$ ,  $B$ ,  $G_{\text{sub}}$ ,  $B_{\text{sub}}$  and  $b_{\text{kg}}$  showing their contribution to the resulting fit following eq. S2 (one representative frame selected for clarity, data  $t = 1200$  s).

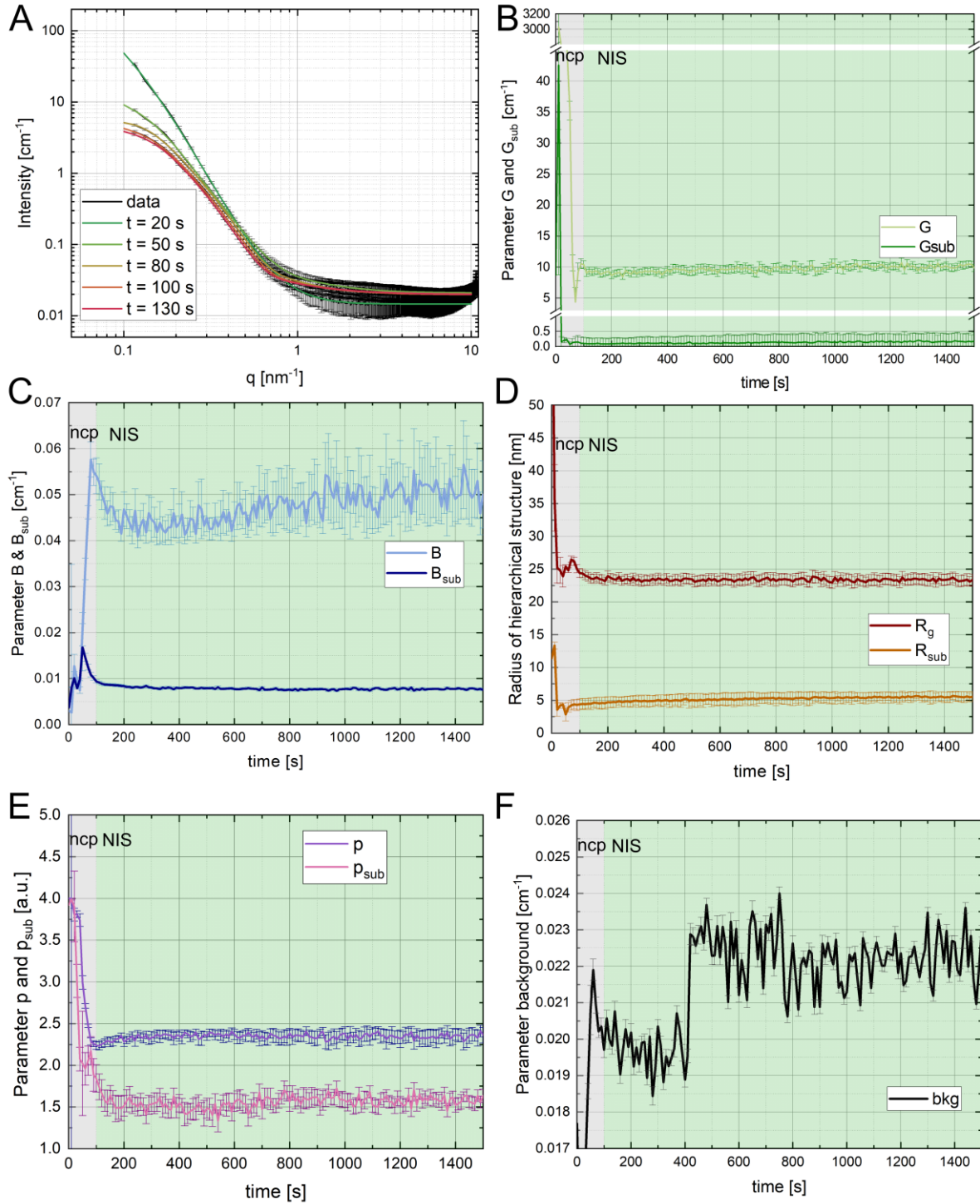


Figure S8: Fitting results of the in-situ SAXS data of the Ni-experiment based on a Beaucage model (Supplementary Note 2, eq. S2); (A) Fits at several times are displayed and show a good agreement with the data within the error bars. The different color shadings mark the distinct phase composition at a given time based on WAXS: grey- no crystalline phases (ncp), light green - NIS (Ni-struvite). The temporal evolution of the distinct fitting parameters is presented in the panels (B-F): (B)  $G$  and  $G_{\text{sub}}$ , (C)  $B$  and  $B_{\text{sub}}$ , (D)  $R_g$  and  $R_{\text{sub}}$ , (E)  $p$  and  $p_{\text{sub}}$ , (F) the time dependent evolution of the background (bkg) parameter is shown.



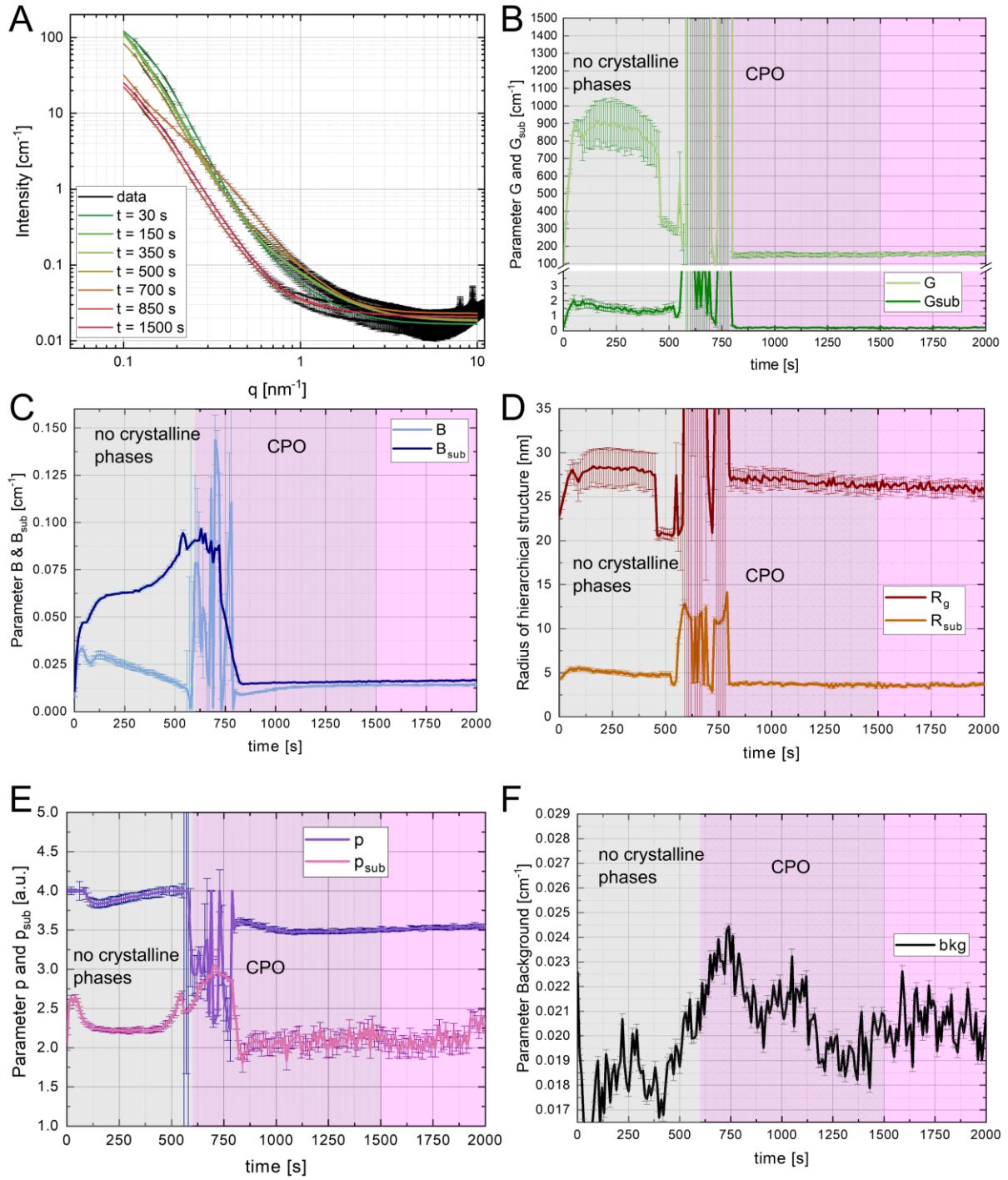


Figure S9: Fitting results of the in-situ SAXS data of the Co-experiment based on a Beaucage model (Supplementary Note 2, eq. S2). The different color shadings mark the distinct phase composition at a given time based on WAXS: grey- no crystalline phases, light pink – CPO, Co-phosphate octahydrate. (A) Fits at selected times are displayed and show a good agreement with the data within the error bars. The temporal evolution of the distinct fitting parameters is presented in the panels (B-F): (B)  $G$  and  $G_{\text{sub}}$ , (C)  $B$  and  $B_{\text{sub}}$ , (D)  $R_g$  and  $R_{\text{sub}}$ , (E)  $p$  and  $p_{\text{sub}}$ . In (F), the time dependent evolution of the background (bkg) parameter is shown.

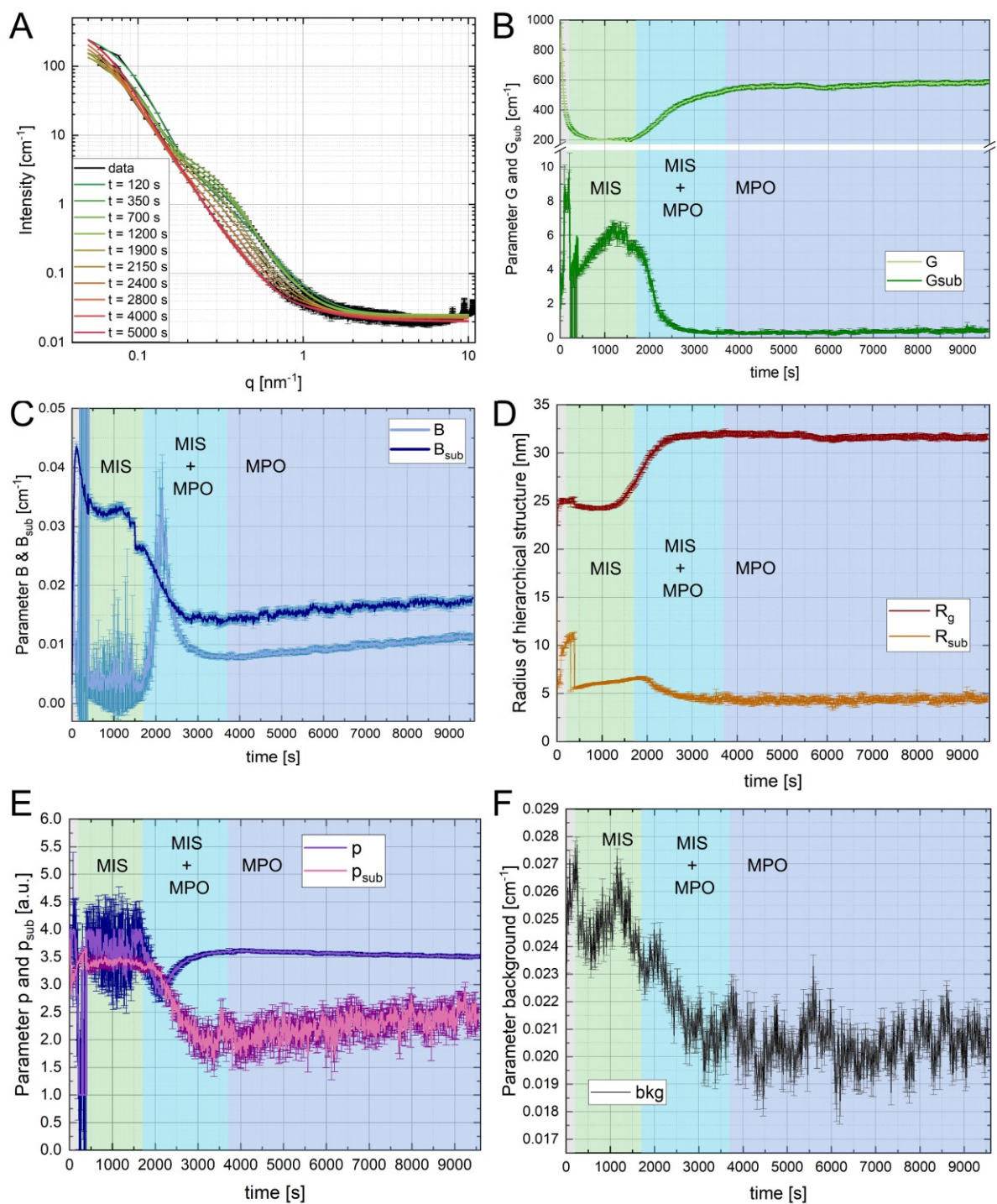


Figure S10: Fitting results of the in-situ SAXS data of the mixed  $\text{Ni}_{50}\text{Co}_{50}$ -experiment based on a Beaucage model (Supplementary Note 2, 3q. S2). The different color shadings mark the distinct phase composition at a given time based on WAXS: grey- no crystalline phases, light green – MIS (M-struvite), light blue- MPO (M-phosphate octahydrate), cyan - MIS+MPO (both phases). (A) Fits of selected times are displayed and show a good agreement with the data within the error bars. The temporal evolution of the distinct fitting parameter is presented in the panels (B-F): (B)  $G$  and  $G_{\text{sub}}$ , (C)  $B$  and  $B_{\text{sub}}$ . (D)  $R_g$  and  $R_{\text{sub}}$ . (E)  $p$  and  $p_{\text{sub}}$ . (F) the time dependent evolution of the background (bkg) parameter is shown.

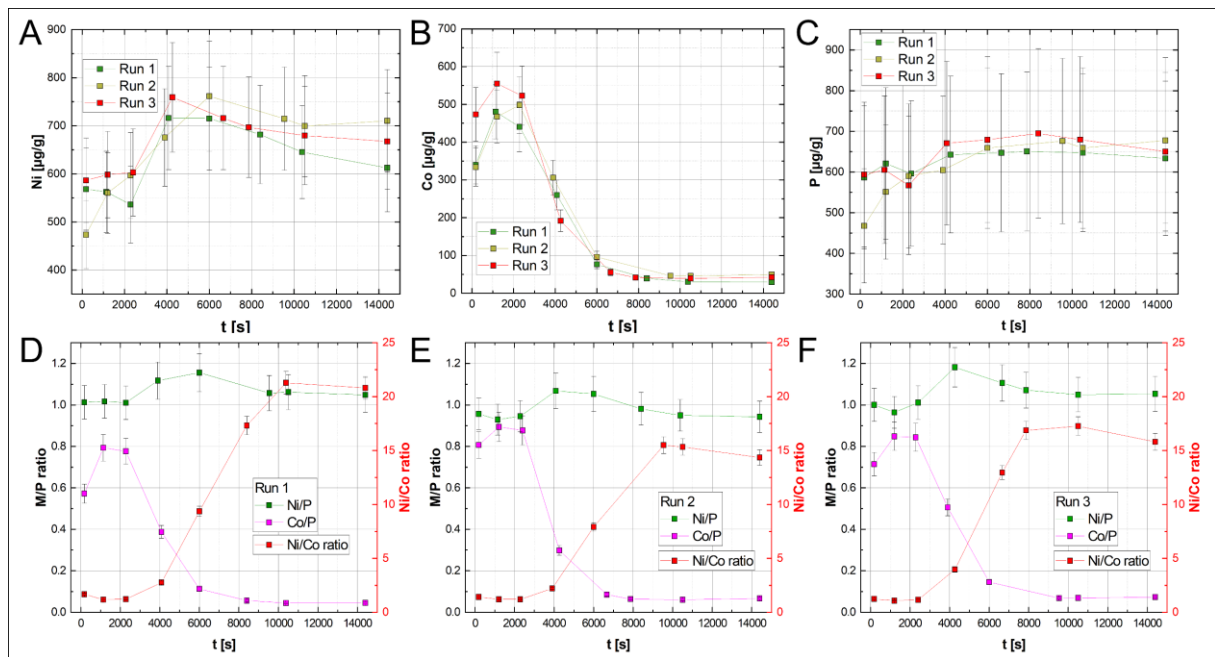


Figure S11: ICP-MS data of the particle-filtered solution with triplicate runs in absolute mass fractions of (A) Ni [ $\mu\text{g/g}$ ], (B), Co [ $\mu\text{g/g}$ ], (C) P [ $\mu\text{g/g}$ ] and their ratio plots of (D) Run 1, (E) Run 2 and (F) Run 3 with error bars.



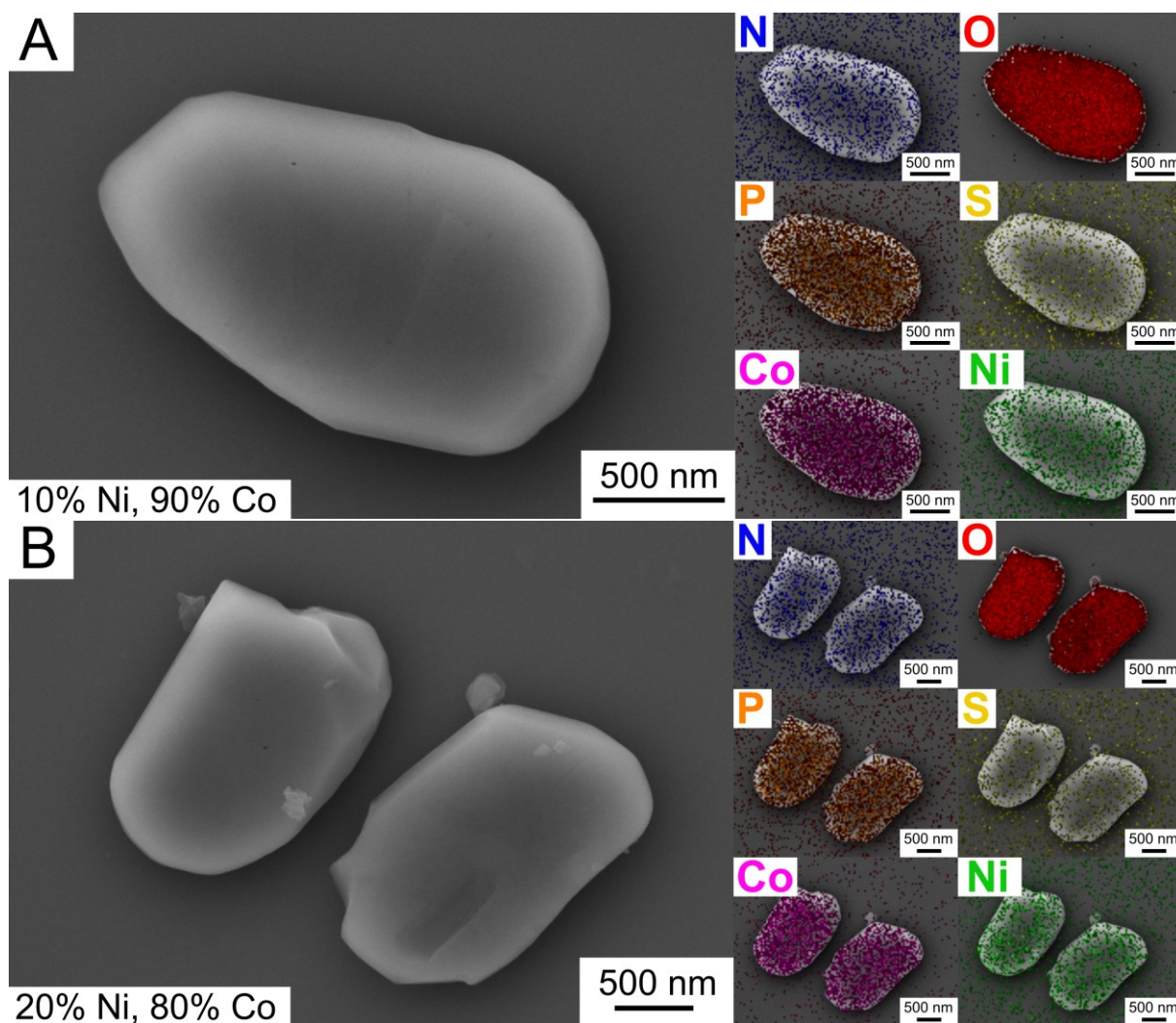


Figure S12: EDS maps of analyzed  $\text{Ni}_x\text{Co}_{1-x}$  solids with  $x = 0.1-0.9$  (A-I, accordingly to the labels) in the experiment. Based on the morphology, size and elemental composition, the  $\text{Ni}_x\text{Co}_{1-x}$ -phosphate octahydrate grains were analyzed. All data to the EDS maps can be found in Table S2. On the left, the SE image of the mapped crystal can be found while on the right, the elemental maps in different colors (N = blue, O = red, P = orange, S = yellow, Co = pink, Ni = green) are displayed. Note the slight zonation occurring especially at low Ni#. At very high content of Ni (Ni# = 90), a Ni-dominated struvite grain was mapped as no M-phosphate octahydrate crystal formed in this sample.

Figure S12, continued:

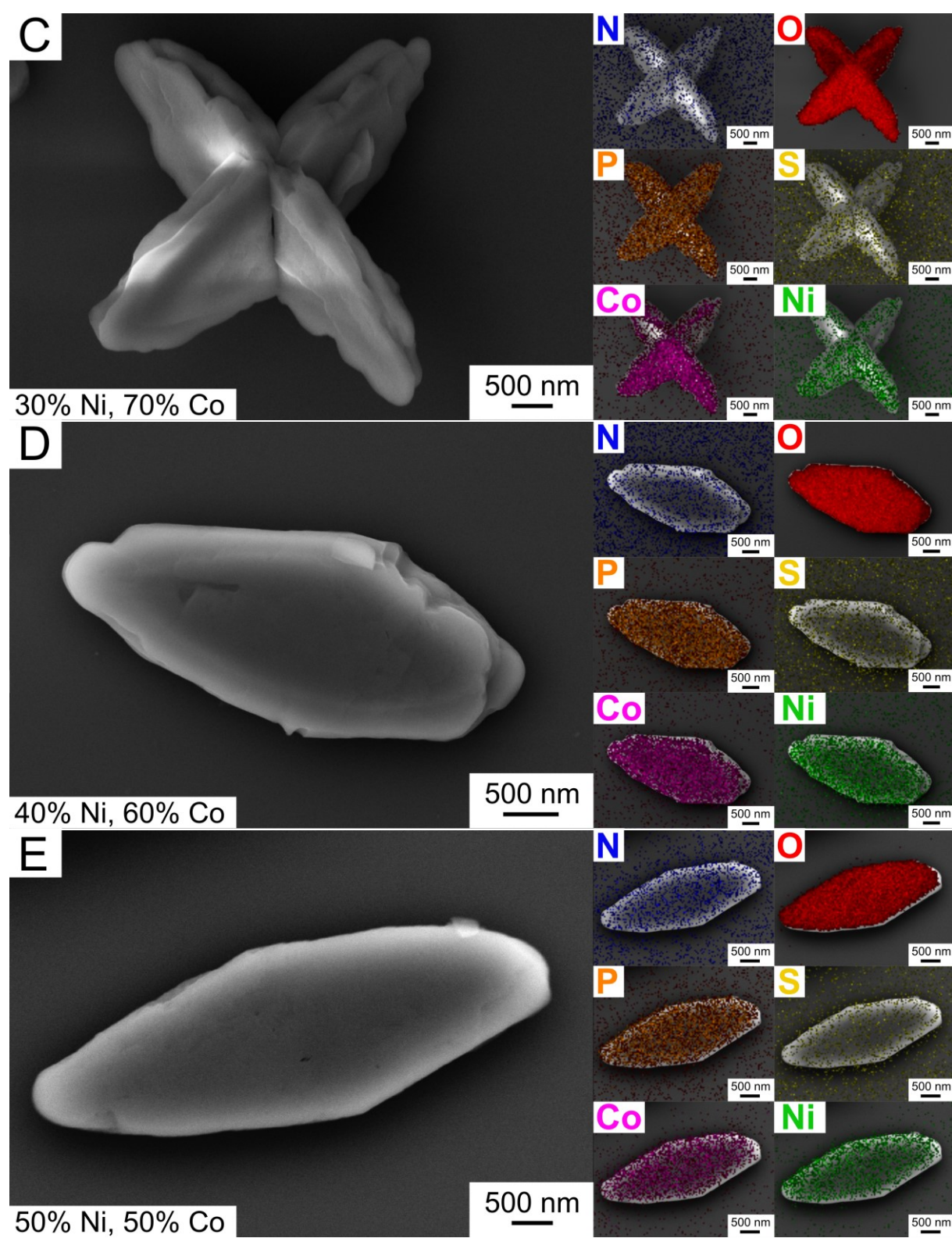




Figure S12 continued:

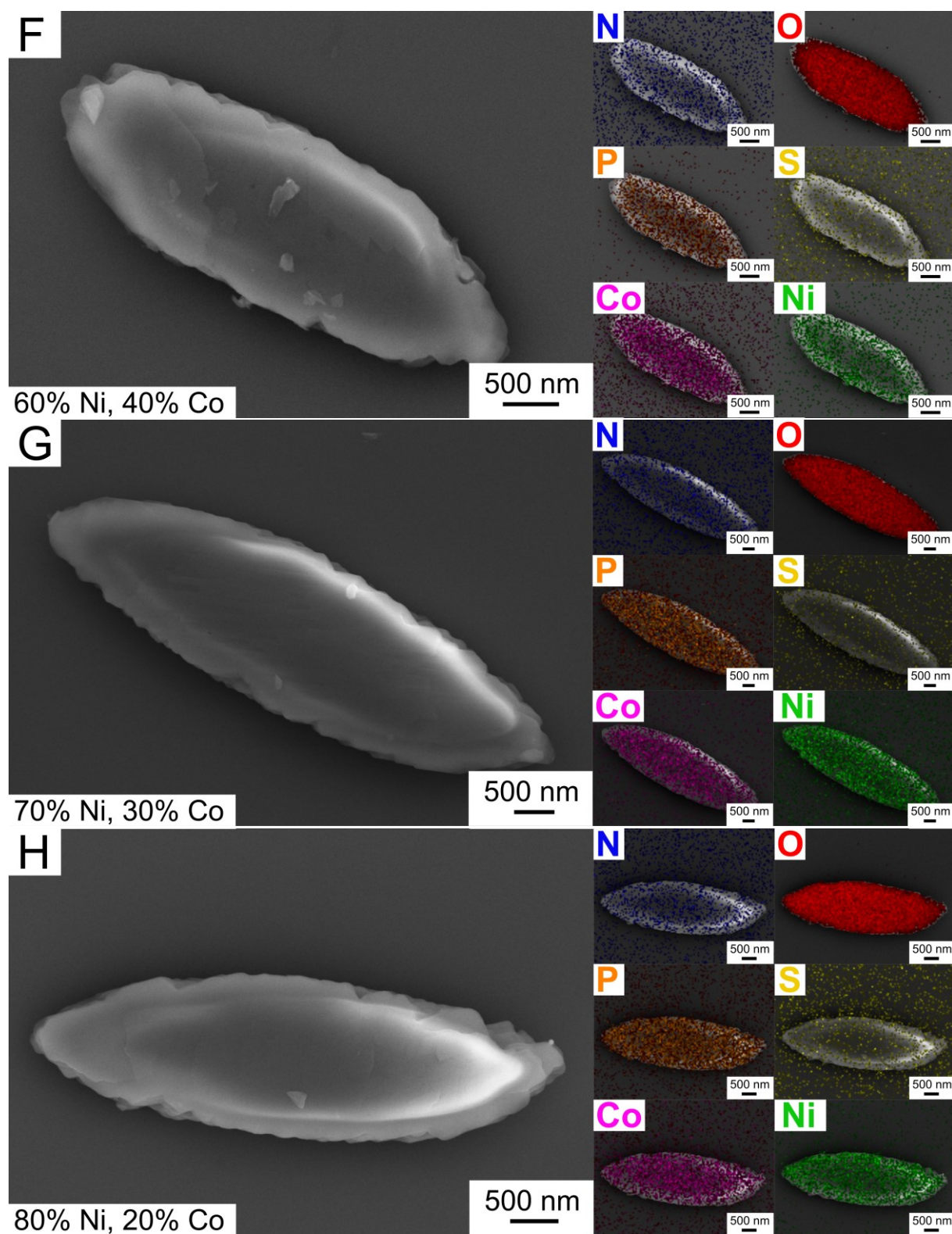
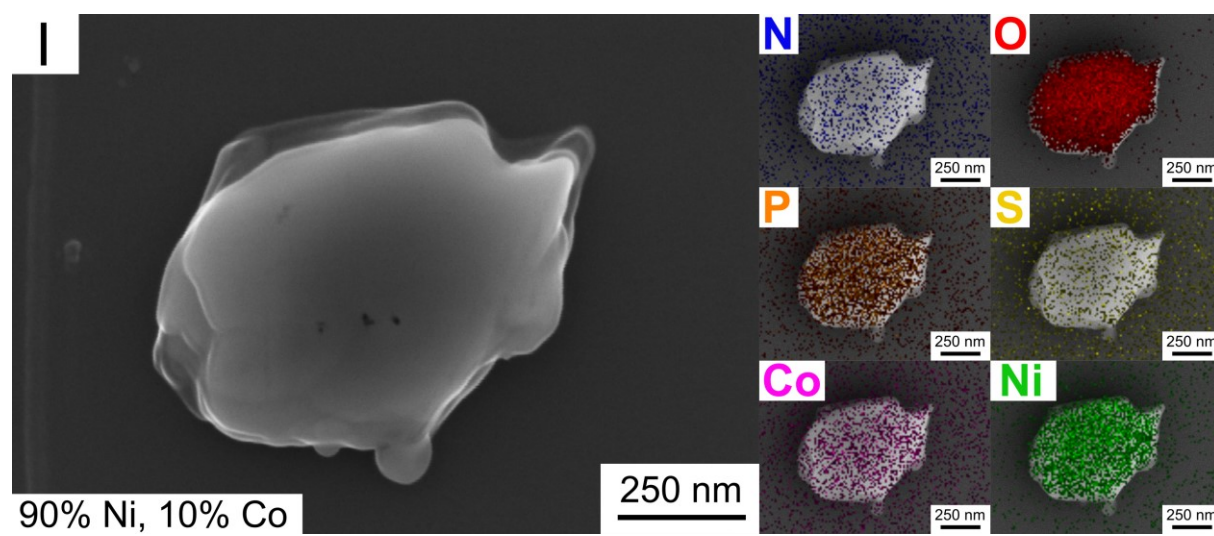


Figure S12, continued:



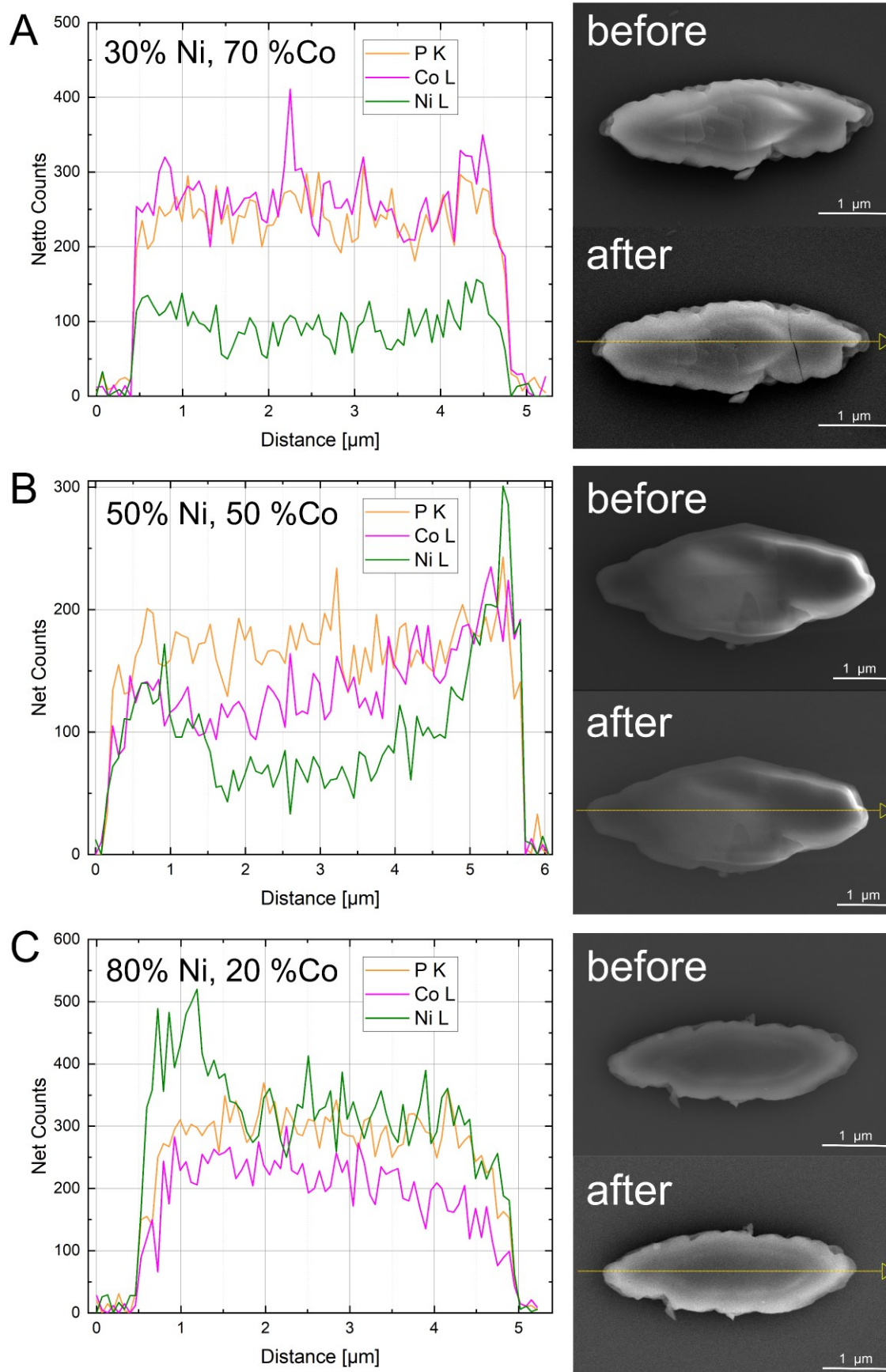


Figure S13: EDS-Line Scans of analyzed  $\text{Ni}_x\text{Co}_{1-x}$  solids with (A)  $x = 30$ , (B)  $x = 50$  and (C)  $x = 80$  in the experiment associated with a SE image before and after the measurement. Based on the morphology, size and elemental composition, only  $\text{Ni}_x\text{Co}_{1-x}$ -phosphate octahydrate grains were analyzed in the line scan measurements.



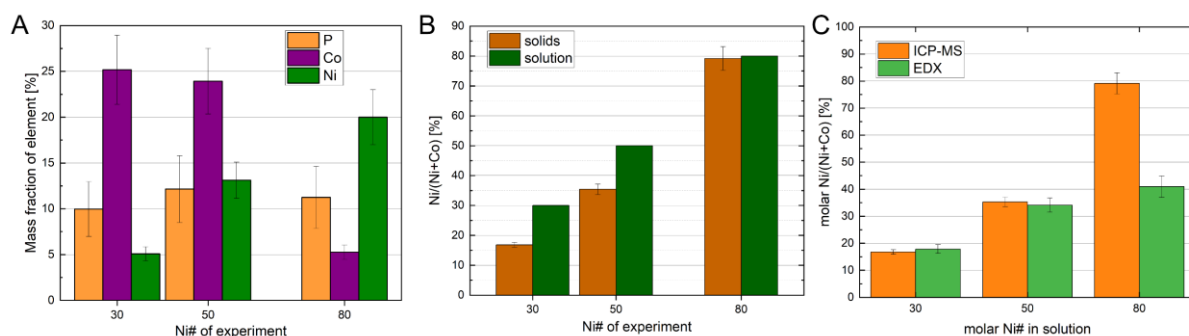


Figure S14: ICP-MS data of Ni, Co and P are displayed in (A) mass fraction of element and (B) in Ni/(Ni+Co) mass ratios from the dissolved solids of the crystallization experiments with distinct mixing ratios of Ni# = 30, 50 and 80. (C) Comparison of elemental information obtained by ICP-MS and the EDS maps of multiple grains: both Ni/(Ni+Co) ratios are in agreement with each other within the uncertainty interval.

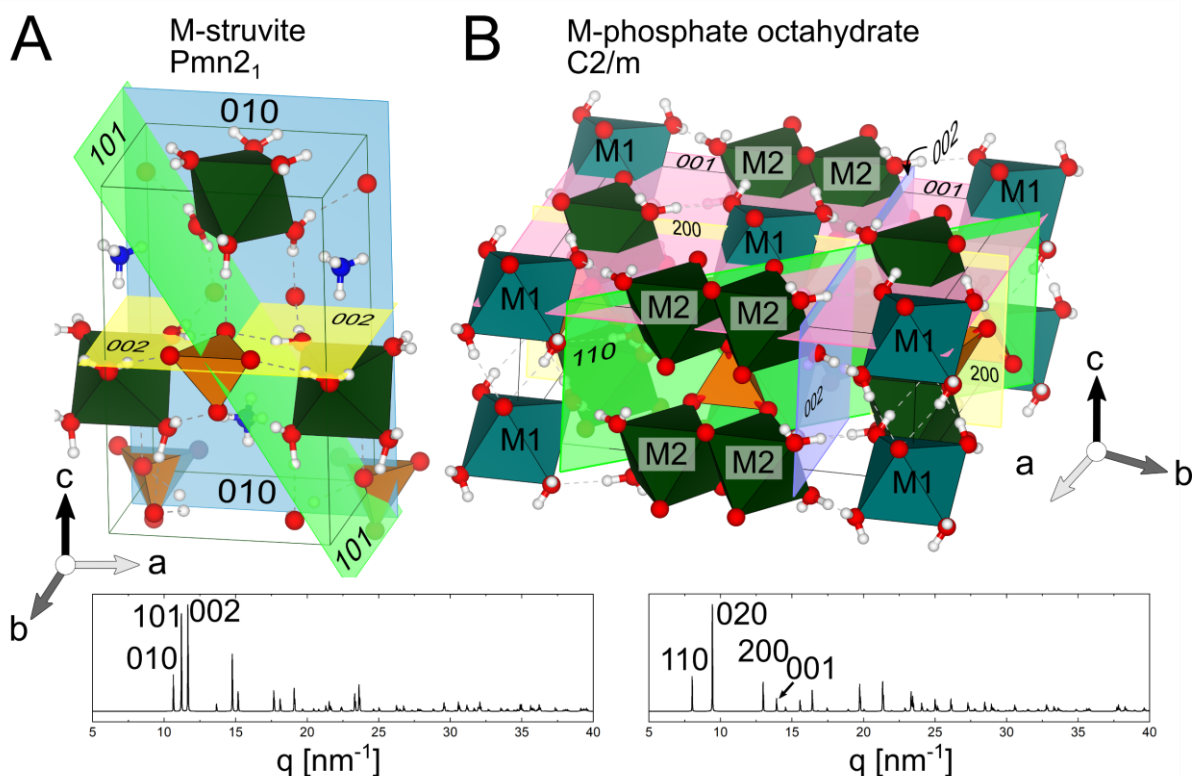


Figure S15: Crystal structures of (A) M-struvite  $Pmn2_1$  and (B) M-phosphate octahydrate  $C2/m$  with distinct colored lattice planes and correspng  $hkl$  reflection in diffractogram below: M-struvite: blue = (010), green = (002), yellow = (002); M-phosphate octahydrate: blue = (002), green = (110), yellow = (200); light red = (001) with two different metal sites M1 resulting in  $M(H_2O)_4O_2$  and M2 resulting in  $M(H_2O)_2O_4$ .

Table S1: Settings of the ICP-MS instrument used for the quantification.

Parameter	ICAP-Q (Thermo Scientific)
Sample introduction	Spray chamber
Nebulizer	PFA – 100 $\mu$ L (Elemental Scientific)
Interface	Ni skimmer + sampler
RF power (W)	1550
Nebulizer gas (L min <sup>-1</sup> )	1.06
Auxillary gas (L min <sup>-1</sup> )	0.65
Isotopes	<sup>31</sup> P, <sup>59</sup> Co, <sup>60</sup> Ni, <sup>62</sup> Ni
Dwell time (s)	0.01
Sweeps	10
Runs	5

Table S2: Summarized EDS data (Ni# = 0.1-0.90, A-H) from multiple mappings of Ni<sub>x</sub>Co<sub>1-x</sub>-phosphate octahydrate crystals with weight and atomic percentage of the respective element; UDL = under detection limit; N and S were measured to identify potential struvite crystals or unreacted species. N as a volatile compound is recorded only in mappings of the last sample (Ni# = 0.9) but it evaporated quickly (within seconds); Note the deviation of the Ni# in solution and Ni# (EDS) in the Ni<sub>x</sub>Co<sub>1-x</sub>-phosphate crystals especially at high Ni# >50%.

A		Element	wt. %	SD	at. %	SD
in solution		N K	UDL	UDL	UDL	UDL
c(Ni <sup>2+</sup> ) [mmol/l]	c(Co <sup>2+</sup> ) [mmol/l]	O K	43.8	0.5	70.6	0.9
10	90	P K	12.3	0.4	10.3	0.3
in crystal		S K	UDL	UDL	UDL	UDL
N	Ni# [%] (EDS)	Co L	39.1	1.0	17.1	0.5
4	10.8	Ni L	4.7	0.6	2.1	0.3
		$\Sigma$	100.0		100.0	
B		Element	wt. %	SD	at. %	SD
in solution		N K	UDL	UDL	UDL	UDL
c(Ni <sup>2+</sup> ) [mmol/l]	c(Co <sup>2+</sup> ) [mmol/l]	O K	45.4	0.7	71.7	1.0
20	80	P K	12.5	0.6	10.2	0.5
in crystal		S K	0.1	0.3	0.0	0.2
N	Ni# [%] (EDS)	Co L	35.0	1.4	15.0	0.6
5	16.9	Ni L	7.1	0.9	3.0	0.4
		$\Sigma$	100.0		100.0	

Table S2, continued:

C		Element	wt. %	SD	at. %	SD
in solution		N K	UDL	UDL	UDL	UDL
c(Ni <sup>2+</sup> ) [mmol/l]	c(Co <sup>2+</sup> ) [mmol/l]	O K	42.8	0.5	70.2	0.8
30	70	P K	10.7	0.3	9.1	0.2
in crystal		S K	0.1	0.2	0.1	0.2
N	Ni# [%] (EDS)	Co L	38.1	0.9	17.0	0.4
5	17.8	Ni L	8.2	0.6	3.7	0.3
		Σ	100.0		100.0	
D		Element	wt. %	SD	at. %	SD
in solution		N K	UDL	UDL	UDL	UDL
c(Ni <sup>2+</sup> ) [mmol/l]	c(Co <sup>2+</sup> ) [mmol/l]	O K	48.4	0.4	74.2	0.6
40	60	P K	11.3	0.3	8.9	0.3
in crystal		S K	UDL	UDL	UDL	UDL
N	Ni# [%] (EDS)	Co L	31.5	0.7	13.1	0.3
5	21.8	Ni L	8.8	0.4	3.7	0.2
		Σ	100.0		100.0	
E		Element	wt. %	SD	at. %	SD
in solution		N K	UDL	UDL	UDL	UDL
c(Ni <sup>2+</sup> ) [mmol/l]	c(Co <sup>2+</sup> ) [mmol/l]	O K	44.3	0.5	70.9	0.8
50	50	P K	12.6	0.3	10.4	0.3
in crystal		S K	UDL	UDL	UDL	UDL
N	Ni# [%] (EDS)	Co L	28.4	1.0	12.3	0.4
6	34.1	Ni L	14.6	0.7	6.4	0.3
		Σ	100.0		100.0	
F		Element	wt. %	SD	at. %	SD
in solution		N K	UDL	UDL	UDL	UDL
c(Ni <sup>2+</sup> ) [mmol/l]	c(Co <sup>2+</sup> ) [mmol/l]	O K	48.9	0.6	74.2	0.9
60	40	P K	12.6	0.5	9.9	0.4
in crystal		S K	UDL	UDL	UDL	UDL
N	Ni# [%] (EDS)	Co L	25.6	1.2	10.6	0.5
6	33.6	Ni L	12.9	0.7	5.3	0.3
		Σ	100.0		100.0	



Table S2, continued:

<b>G</b>		<b>Element</b>	<b>wt. %</b>	<b>SD</b>	<b>at. %</b>	<b>SD</b>
<b>in solution</b>		N K	UDL	UDL	UDL	UDL
<b>c(Ni<sup>2+</sup>)</b> <b>[mmol/l]</b>	<b>c(Co<sup>2+</sup>)</b> <b>[mmol/l]</b>	O K	48.5	0.7	74.4	1.0
<b>70</b>	<b>30</b>	P K	11.1	0.6	8.8	0.5
<b>in crystal</b>		S K	UDL	UDL	UDL	UDL
<b>N</b>	<b>Ni# [%] (EDS)</b>	Co L	25.2	1.3	10.5	0.5
<b>6</b>	<b>37.7</b>	Ni L	15.2	0.8	6.3	0.3
		Σ	100.0		100.0	
<b>H</b>		<b>Element</b>	<b>wt. %</b>	<b>SD</b>	<b>at. %</b>	<b>SD</b>
<b>in solution</b>		N K	UDL	UDL	UDL	UDL
<b>c(Ni<sup>2+</sup>)</b> <b>[mmol/l]</b>	<b>c(Co<sup>2+</sup>)</b> <b>[mmol/l]</b>	O K	48.6	0.6	74.1	1.0
<b>80</b>	<b>20</b>	P K	12.6	0.6	9.9	0.4
<b>in crystal</b>		S K	UDL	UDL	UDL	UDL
<b>N</b>	<b>Ni# [%] (EDS)</b>	Co L	23.0	1.2	9.5	0.5
<b>6</b>	<b>40.9</b>	Ni L	15.8	0.7	6.6	0.3
		Σ	100.0		100.0	
<b>I</b>		<b>Element</b>	<b>wt. %</b>	<b>SD</b>	<b>at. %</b>	<b>SD</b>
<b>in solution</b>		N K	0.2	0.4	0.3	0.7
<b>c(Ni<sup>2+</sup>)</b> <b>[mmol/l]</b>	<b>c(Co<sup>2+</sup>)</b> <b>[mmol/l]</b>	O K	45.2	0.5	71.1	0.9
<b>90</b>	<b>10</b>	P K	13.3	0.4	10.8	0.3
<b>in crystal</b>		S K	UDL	UDL	UDL	UDL
<b>N</b>	<b>Ni# [%] (EDS)</b>	Co L	9.5	1.2	4.1	0.5
<b>6</b>	<b>77.0</b>	Ni L	31.8	0.7	13.6	0.3
<b>struvite crystal!</b>		Σ	100.0		100.0	

Table S3: ICP-MS data of particle-filtered solution from crystallization experiments in triplicate runs. Data is given with relative measurement uncertainty of  $U_{rel}$  ( $k = 2$ ) resulting in the relative errors of 30% for P and 15% for Ni and Co, respectively. LOD – limit of detection, LOQ – limit of quantitation, Bkg – background.

Run	sampling time	P	$\Delta P$	Co	$\Delta Co$	Ni	$\Delta Ni$
	s	$\mu g/g$	$\mu g/g$	$\mu g/g$	$\mu g/g$	$\mu g/g$	$\mu g/g$
1	180	594	178	51	340	85	568
	1140	605	182	72	480	84	563
	2280	567	170	66	441	80	536
	4080	671	201	39	260	107	716
	6000	679	204	11	76	107	715
	8400	695	208	6	39	102	682
	10380	680	204	5	30	97	645
	14400	650	195	4	29	92	613
	DAP (NH <sub>4</sub> ) <sub>2</sub> HPO <sub>4</sub> Bkg	2619	786		LOD		LOD
	NiCo(Ni <sub>50</sub> Co <sub>50</sub> SO <sub>4</sub> ) Bkg	LOD		406	2706	421	2806
2	180	468	140	50	334	71	473
	1200	551	165	70	467	84	560
	2280	590	177	75	498	89	597
	3900	605	181	46	306	101	676
	6000	659	198	14	96	114	762
	9540	676	203	7	46	107	715
	10500	659	198	7	46	105	699
	14400	678	203	7	50	107	710
	DAP (NH <sub>4</sub> ) <sub>2</sub> HPO <sub>4</sub> Bkg	2463	739		LOD		0
	NiCo(Ni <sub>50</sub> Co <sub>50</sub> SO <sub>4</sub> ) Bkg	LOD		421	2804	423	2822
3	180	587	176	71	473	88	587
	1200	621	186	83	555	90	598
	2400	596	179	78	523	90	603
	4260	643	193	29	192	114	759
	6660	647	194	8	55	107	716
	7860	651	195	6	41	105	697
	10500	648	194	6	39	102	680
	14400	634	190	6	42	100	668
	DAP (NH <sub>4</sub> ) <sub>2</sub> HPO <sub>4</sub> Bkg	2566	770		LOD		LOD
	NiCo(Ni <sub>50</sub> Co <sub>50</sub> SO <sub>4</sub> ) Bkg	LOD		430	2869	432	2880
-	LOD	11		0.01		0.02	
-	LOQ	21		0.03		0.05	

Table S4: ICP-MS data of dissolved (Ni<sub>x</sub>Co<sub>1-x</sub>)<sub>3</sub>(PO<sub>4</sub>)<sub>2</sub> crystals in triplicate runs. Data is given with relative measurement uncertainty of  $U_{rel}$  ( $k = 2$ ) resulting in the relative errors of 30% for P and 15% for Ni and Co, respectively. LOD – limit of detection, LOQ – limit of quantitation, Bkg – background.

Analyte	P	$\Delta P$	Co	$\Delta Co$	Ni	$\Delta Ni$	$\frac{Ni}{Ni + Co}$	$\Delta[\frac{Ni}{Ni+Co}]$
	%	%	%	%	%	%	% / %	% / %
Ni <sub>30</sub> Co <sub>70</sub> -mixture	10.0	3.0	25.2	3.8	5.1	0.8	16.8	0.8
Ni <sub>50</sub> Co <sub>50</sub> -mixture	12.1	3.6	23.9	3.6	13.1	2.0	35.4	1.8
Ni <sub>80</sub> Co <sub>20</sub> -mixture	11.3	3.4	5.3	0.8	20.0	3.0	79.2	4.0
LOD	0.09		<0.01		<0.01			
LOQ	0.25		<0.01		<0.01			

## References:

1. Mastronarde, D. N., Automated electron microscope tomography using robust prediction of specimen movements. *Journal of Structural Biology* **2005**, *152* (1), 36-51.
2. Pettersen, E. F.; Goddard, T. D.; Huang, C. C.; Couch, G. S.; Greenblatt, D. M.; Meng, E. C.; Ferrin, T. E., UCSF Chimera--a visualization system for exploratory research and analysis. *J Comput Chem* **2004**, *25* (13), 1605-12.
3. Newville, M.; Stensitzki, T.; Allen, D.; Ingargiola, A., *LMFIT: Non-Linear Least-Square Minimization and Curve-Fitting for Python*. 2014.
4. (DIN), D. I. f. N., DIN ISO 11843-2. In *Capability of detection - Part 2: Methodology in the linear calibration case (ISO 11843-2:2000)*. Beuth Verlag: 2006; p 35.
5. Kragten, J., Calculating Standard Deviations and Confidence Intervals with a Universally Applicable Spreadsheet Technique. *Analyst* **1994**, *119*, 2161-2165.
6. Beaucage, G., Approximations Leading to a Unified Exponential/Power-Law Approach to Small-Angle Scattering. *J. Appl. Cryst.* **1995**, *28*, 717-728.
7. Beaucage, G., Small-Angle Scattering from Polymeric Mass Fractals of Arbitrary Mass-Fractal Dimension. *J. Appl. Cryst.* **1996**, *29*, 134-146.
8. Beaucage, G.; Kammler, H. K.; Pratsinis, S. E., Particle size distributions from small-angle scattering using global scattering functions. *Journal of Applied Crystallography* **2004**, *37* (4), 523-535.
9. Porod, G., Die Röntgenkleinwinkelstreuung von dichtgepackten kolloiden Systemen. *Kolloid-Zeitschrift* **1951**, *124* (1), 51-57.
10. Porod, G., Die Röntgenkleinwinkelstreuung von dichtgepackten kolloiden Systemen. *Kolloid-Zeitschrift* **1952**, *125* (1), 51-57.
11. Guinier, A.; Fournet, G., *Small Angle Scattering of X-rays*. John Wiley & Sons: New York, NY, 1955.